Materials Science Forum
ISSN: 1662-9752, Vol. 1182, pp 91-102
doi:10.4028/p-Nfg58d

Submitted: 2026-01-19
Revised: 2026-02-16
Accepted: 2026-02-17
Online: 2026-04-10

Numerical Modelling of Intimate Contact for Thermoplastic Composite Joints

WAROQUIER Pierre[1,2,a*], LEVY Arthur[1,b], LE CORRE Steven[1,c], BAILLEUL Jean-Luc[1,d], SERRA Joël[2,e], BERTEVAS Erwan[2,f]

[1]Nantes Université, CNRS, Laboratoire de Thermique et Énergie de Nantes, LTeN, UMR6607, F-44000, Nantes, France

[2]Institut de Recherche Technologique Jules Verne, 1 Mail des 20000 Lieues, 44343 Bouguenais, France

[a*] pierre.waroquier@univ-nantes.fr (*corresponding author), [b]arthur.levy@univ-nantes.fr, [c]steven.lecorre@univ-nantes.fr, [d]jean-luc.bailleul@univ-nantes.fr, [e]joel.serra@irt-jules-verne.fr, [f]erwan.bertevas@irt-jules-verne.fr

Keywords: Composites, Thermoplastic, Welding, Intimate Contact, Adhesion, Squeeze Flow

Abstract. High-performance thermoplastic polymers paved the way for new fast manufacturing processes, including welding. In order to obtain optimal bonding of the substrates, an adhesion step is required, governed by two main phenomena: intimate contact and healing. While healing has been widely explored, theorized, and is starting to be understood, prediction and characterization of the degree of intimate contact is still a challenge. After a review of squeeze flow models for intimate contact, along with the expressions of the analytical solutions for a Newtonian and a shear-thinning fluid modeled by power law, a finite element model is presented in order to observe the influence of asperity geometry, fluid behavior, and other assumptions on the evolution of the degree of intimate contact.

Introduction

The use of thermoplastic resins in carbon fiber-reinforced polymer (CFRP) materials has received increasing interest over the years due to promising mechanical and chemical properties. In addition to simple storage conditions prior to processing, thermoplastics can also be remelted, offering reprocessability, repairability, and potential recyclability. This asset allowed new consolidation processes and joining techniques [1, 2]. In any thermoplastic composite manufacturing or joining process, adhesion is critical to obtain the best mechanical properties for the final composite part. In this work, adhesion is considered at a thermoplastic composite interface. This adhesion can be between unidirectional tapes as in the Automated Fiber Placement (AFP) process, or between neat polymer and composite substrate (overmolding), or even between composite substrates (welding). With increasing demand for CFRP, manufacturing processes are becoming fast or even continuous. For instance, the characteristic process times of AFP, overmolding, and conduction welding are approximately, 200 ms, 1 s, and 10 s, respectively.

For fast manufacturing processes, adhesion has only a short time to occur. Adhesion can be decomposed into two phenomena: intimate contact and healing. At the beginning, two molten substrates (whether unidirectional tapes, raw polymer films, etc...) with initial surface roughness are considered. The first step consists in flattening the surface asperities by applying pressure to the substrates. This aims to attain optimal surface contact, defined as ”intimate contact”. The degree of intimate contact D_{ic} is thus defined as the ratio between the area of contact and the total area of the substrate surface. D_{ic} is highly dependent on the pressure applied, processing temperature, and contact time. If asperities do not flatten sufficiently, contact will be limited and remain incomplete as the temperature at the interface decreases rapidly.

As soon as some asperities come into contact, interdiffusion of macromolecular chains can occur by ”reptation” movements of the chains, as originally theorized by De Gennes in 1971 [3]. The

healing phase corresponds to the progressive recovery of the strength of the interface as a result of the interdiffusion of the chains across this newly created interface. Wool and O'Connor [4] introduced the degree of healing, $D_h = \sigma/\sigma_\infty$, where σ is the strength of the interfacial fracture and σ_∞ the strength of the interfacial fracture of the virgin material. The degree of healing enables the evaluation of strength recovery at the interface. For thermoplastic polymers, the degree of healing is modeled according to the polymer diffusion theory as

$$D_h \propto \left(\frac{t}{t_w}\right)^{1/4} \tag{1}$$

where t_w is the welding time, which corresponds to a full recovery of interface strength.

Although healing theory has been extensively studied for long adhesion times [5], intimate contact, which is predominant for fast processes [6], remains difficult to predict accurately. The most common analytical models for evaluating the degree of intimate contact are based on squeeze flow [7, 8, 9]. More recently, alternative intimate contact models, based on Darcy flow [10, 11] have shown a new way to consider the intimate contact phenomenon with resin "percolation" of the interfacial voids. Other models considering bubble or void growth in molten thermoplastics may also be useful to predict intimate contact [12, 13]. The development of intimate contact can also be limited by surrounding gas or degassed chemicals from molten resin or fiber sizing that can remain trapped between asperities.

In fast manufacturing processes, intimate contact and healing are coupled; Butler et al. [14] define the degree of bonding, D_b, to evaluate the resulting bond strength. Assuming that D_{ic} is a sufficient parameter to calculate the adhesion strength, the expression of D_b is given by

$$D_b(t) = D_{ic}(0)D_h(t) + \int_0^t D_h(t-\tau)\dot{D_{ic}}(\tau)d\tau \tag{2}$$

When D_b is equal to 1, interface properties are fully recovered. Fig. 1 represents the different stages of a fast adhesion with regard to these phenomena. The aim of this work is to obtain a realistic intimate

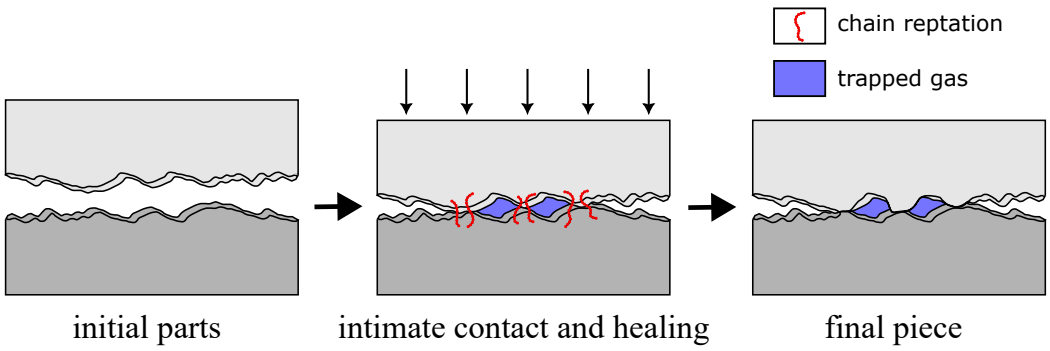

Fig. 1: Mechanisms governing short-time adhesion.

contact model. The methodology consists in numerically solving the flow of an asperity at the interface. A FreeFEM++ numerical finite element model based on Newtonian and non-Newtonian squeeze flow for different geometries is developed. It is then compared to common intimate contact squeeze flow analytical solutions.

Review of Intimate Contact Models with Squeeze Flow

Squeeze flow models have historically been the first to be used in predicting intimate contact for thermoplastic composites. In 1985, Dara and Loos [7] first considered the initial roughness of a unidirectional tape as a succession of non-uniform rectangles representing the tows of a unidirectional tape.

This first model was then simplified two years later by Lee and Springer [8], who replaced the rectangles of different shapes with evenly spaced and uniform rectangles. This model is the most commonly used in the literature due to the low number of input parameters required for it to give an estimation of the degree of intimate contact. The model was then updated by Mantell and Springer [15] to consider time-dependency of pressure, temperature, and viscosity. In order to describe the geometry of squeezed asperities more precisely, Yang and Pitchumani [9] developed a new rectangle model based on a Cantor set fractal description of roughness. Although these models are widely used in the field of thermoplastic polymers, they are based on strong hypotheses:

- The asperities are rectangles, wider than they are tall, in order to comply with the lubrication assumption. Squeezed rectangles are thus supposed to remain rectangles at every time.
- The rheological behavior of the thermoplastic polymer fluid is considered to be Newtonian, but its real behavior tends to be non-Newtonian (shear-thinning fluid), depending on the interface squeezing velocity.
- Other physical and chemical aspects such as wetting and air-trapping are not taken into account while modeling the phenomenon.

Governing equations of squeeze flow. In order to describe the evolution of intimate contact, asperities are modeled as rectangles, as schematized in Fig. 2. An incompressible two-dimensional fluid is considered. Instead of working with the roughness of the two surfaces, only the asperity of a single surface is represented. This equivalent asperity is squeezed onto a flat rigid surface. This assumption is common in the literature and is based on Greenwood and Williamson's work [16]. The asperity is assumed to be composed only of resin, an assumption made based on the fact that studied substrates have a polymer film at their surface in order to enhance adhesion when welded. It is supposed that the body and gravitational forces are neglected, with the prevalence of viscous forces. With a Reynold number, Re, much smaller than unity, inertia effects can also be neglected. No-slip boundary conditions on the upper and lower sides of the rectangle is considered. Additionally, the lubrication assumption is expressed, hence, the height $h(t)$ of the rectangle is supposed to be smaller than the width $L(t)$, at every time. The Navier-Stokes equations (i.e. the momentum and incompressibility equations) are written

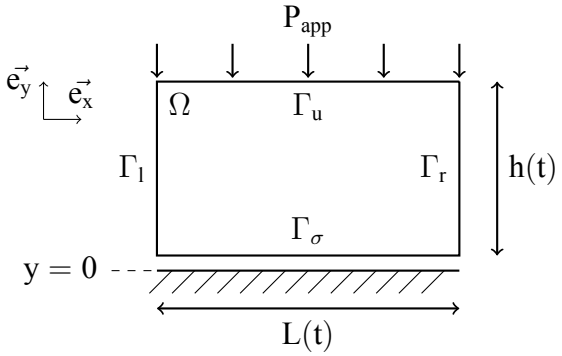

Fig. 2: Schematic of the squeeze flow problem for intimate contact. The domain of the problem is Ω.

in this case as

$$\begin{cases} \vec{\nabla} \cdot \underline{\underline{\sigma}} = \vec{0} \ \text{ on } \ \Omega \\ \vec{\nabla} \cdot \vec{u} = 0 \ \text{ on } \ \Omega \\ \oint_{\Gamma_u} \left(\underline{\underline{\sigma}} \cdot \vec{n} \right) \cdot \vec{e_y} = P_{app} \end{cases} \tag{3}$$

with $\underline{\underline{\sigma}} = 2\mu\underline{\underline{D}} - p\underline{\underline{I}}$ the two-dimensional stress tensor of the fluid, where $\underline{\underline{D}}$ is the strain rate tensor, μ is the viscosity modeled by the Ostwald-de Waele power law $\mu = K\dot{\gamma}^{n-1}$, where K and n are the flow consistency and behavior indices, respectively. p and $\vec{u}$ are the pressure and the velocity vector of the studied fluid. The third equation is used to consider the constant lineic load P_{app} applied onto the substrate. The upper boundary Γ_u moves at $\dot{h}$ velocity and is obtained thanks to the lineic load P_{app}.

The solutions of this Stokes problem for a Newtonian and a power law fluid can be found and are summarized in Fig. 3 with free-slip and no-slip boundary conditions.

Analytical solutions for intimate contact. In the case of the squeeze flow models, the degree of intimate contact D_{ic} is defined as

$$D_{ic} = \frac{L}{L_\infty} \tag{4}$$

where L_∞ is the spatial period between asperities. For simple compression and squeeze flow, if the lubrication assumption is considered, mass conservation gives $L = \frac{L_0 h_0}{h}$, where L_0 and h_0 are the initial height and width of the rectangle, respectively. L can thus be replaced in Eq. 4:

$$D_{ic} = \frac{L_0 h_0}{h L_\infty} \tag{5}$$

From Eq. 5 and the solutions expressed in Fig. 3, it is possible to find an evolution law for the degree of intimate contact for each case. For non-isothermal processes, it is more convenient to adopt an instantaneous approach. The rate of intimate contact $\dot{D}_{ic}$ is expressed as a function of the degree of intimate contact D_{ic}, along with the geometrical and process parameters. The corresponding expression of $\dot{D}_{ic}$ is

$$\dot{D}_{ic} = -\frac{L_0 h_0}{L_\infty}\frac{\dot{h}}{h^2} = -\frac{\dot{h} L_\infty D_{ic}^2}{L_0 h_0} \tag{6}$$

The evolution law of the simple compression of a rectangle with a shear-thinning fluid is

$$\dot{D}_{ic} = D_{ic}^{1-\frac{1}{n}}\left(\frac{-P_{app}}{L_\infty 2^{n+1} K}\right)^{\frac{1}{n}} \propto \left(-\frac{P_{app}}{K}\right)^{\frac{1}{n}} D_{ic}^{1-\frac{1}{n}} \tag{7}$$

If the fluid is Newtonian, the flow behavior index n is equal to 1 and $\dot{D}_{ic}$ does not depend on D_{ic}. Similarly, the evolution law of the degree of intimate contact for the squeeze flow of a rectangle with a shear-thinning fluid is

$$\dot{D}_{ic} = D_{ic}^{\frac{-(n+3)}{n}}\frac{L_\infty}{L_0 h_0}\frac{2n}{n+1}\left[\left(\frac{L_0 h_0}{2L_\infty}\right)^{\frac{1+2n}{n}}\left(1-\frac{n}{1+2n}\right)\right]\left(\frac{(n+1)P_{app}}{2\mu}\frac{1}{\left(\frac{L_\infty}{2}\right)^{n+2}\left(\frac{1}{n+2}-1\right)}\right)^{\frac{1}{n}} \tag{8}$$

In this case, $\dot{D}_{ic}$ is proportional to $(P_{app}/K)^{\frac{1}{n}} D_{ic}^{\frac{-(n+3)}{n}}$ and when $n = 1$, the result is the same as reported in the literature [8], with $\dot{D}_{ic} \propto (P_{app}/K)^{\frac{1}{n}} D_{ic}^{-4}$. For both simple compression and squeeze flow configurations, $\dot{D}_{ic}$ appears to be proportional to a power of D_{ic} and $(P_{app}/K)^{\frac{1}{n}}$. A generalized evolution model is thus suggested with

$$\dot{D}_{ic} \propto \left(\frac{P_{app}}{K}\right)^{\frac{1}{n}} (D_{ic})^{\alpha} \tag{9}$$

where α is an evolution index that may vary with asperity geometry and boundary conditions.

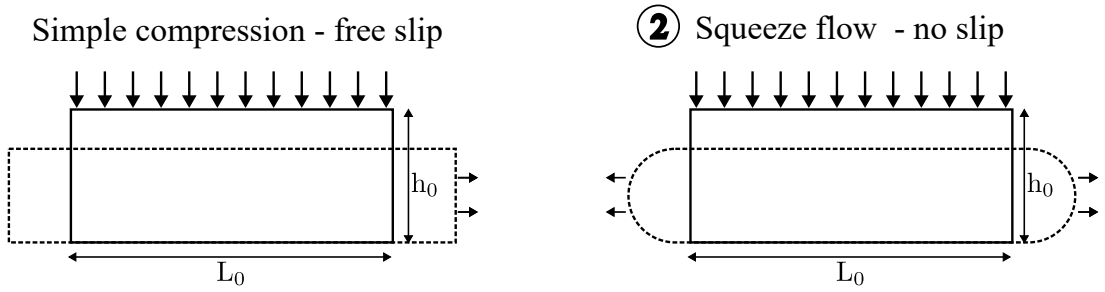

① Newtonian fluid:

$$\begin{cases} u_x = -\frac{\dot{h}}{h}x \\ u_y = \frac{\dot{h}}{h}y \\ p = -2\mu\frac{\dot{h}}{h} \\ \dot{h} = \frac{h^2 P_{app}}{4\mu L_0 h_0} \end{cases}$$

① Shear-thinning fluid:

$$\begin{cases} u_x = -\frac{\dot{h}}{h}x \\ u_y = \frac{\dot{h}}{h}y \\ p = 2^n K\left(-\frac{\dot{h}}{h}\right)^n \\ \dot{h} = -h\left(\frac{-P_{app}h}{2^{n+1}KL_0h_0}\right)^{\frac{1}{n}} \end{cases}$$

② Newtonian fluid:

$$\begin{cases} u_x = x(y^2 - hy)\frac{6\dot{h}}{h^3} \\ u_y = \frac{\dot{h}}{h}y \\ p = 6\mu\frac{\dot{h}}{h^3}\left(x^2 - \left(\frac{L_0h_0}{2h}\right)^2\right) \\ \dot{h} = \frac{h^6 P_{app}}{\mu(L_0h_0)^3} \end{cases}$$

② Shear-thinning fluid:

$$\begin{cases} u_x = \left(\frac{h\dot{x}}{2\left(\frac{h}{2}\right)^{\frac{1+2n}{n}}\left(1-\frac{n}{1+2n}\right)}\right)\left[\left(-y+\frac{h}{2}\right)^{\frac{1+n}{n}} - \left(\frac{h}{2}\right)^{\frac{1+n}{n}}\right] \\ u_y = \frac{\dot{h}}{h}y \\ p = -\frac{K}{n+1}\left(-\frac{\dot{h}(n+1)}{2n}\frac{1}{\left(\frac{h}{2}\right)^{\frac{1+2n}{n}}\left(1-\frac{n}{1+2n}\right)}\right)^n\left(x^{n+1} - \left(\frac{L_0h_0}{2h}\right)^{n+1}\right) \\ \dot{h} = \frac{-2n}{n+1}\left[\left(\frac{h}{2}\right)^{\frac{1+2n}{n}}\left(1-\frac{n}{1+2n}\right)\right]\left(\frac{(n+1)P_{app}}{2\mu}\frac{1}{\left(\frac{L_0h_0}{2h}\right)^{n+2}\left(\frac{1}{n+2}-1\right)}\right)^{\frac{1}{n}} \end{cases}$$

Fig. 3: Solutions of the Stokes problem for a rectangle with free-slip **(1)** and no-slip **(2)** boundary conditions for Newtonian and non-Newtonian fluids. The velocity of the upper boundary is $\dot{h}$.

Finite Element Model for Intimate Contact

In order to determine the missing constant α in the evolution law given by Eq. 9, a finite element study of the flow is investigated.

Resolution domain and numerical implementation. An updated Lagrangian approach is considered. The Stokes problem in Eq. 3 is solved with an explicit iterative time integration scheme for $\vec{u}$, u on domain Ω and $\dot{h}$. Space integration is handled with standard P2/P1 finite element method in

FreeFEM++. The mesh is then moved explicitly according to the displacement field $\vec{u}\delta t$ where δt fulfills the Courant-Friedrichs-Lewy convergence condition. Fig. 4a illustrates the initial full shape of an example geometry, in this case a triangle asperity. Fig. 4b presents the computed symmetry that is solved numerically. The mesh is composed of triangular elements.

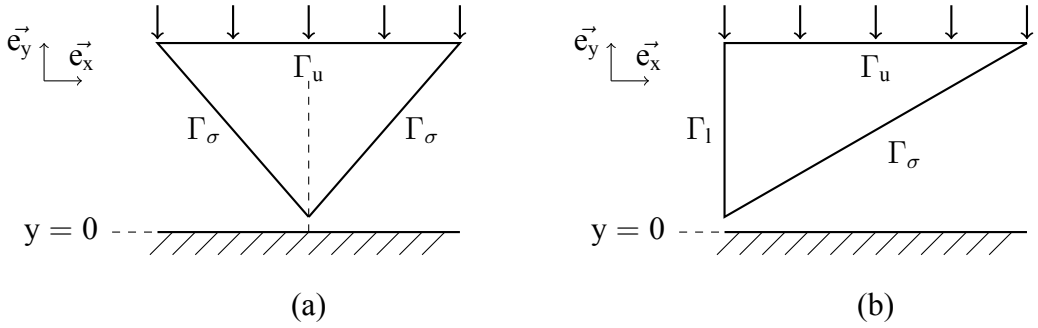

Fig. 4: (a) Resolution domain for a triangular asperity with a central axis of symmetry represented by Γ_l. (b) Simplification of the domain using symmetrical considerations. The effective length of Γ_u is twice as small even if the visual ratio is conserved in this schematic.

Contact between the asperity and the origin surface $y = 0$ is handled by implicit penalization over Γ_σ with the penalization force vector $\vec{f_{pen}}$ defined as

$$\begin{cases} \vec{f_{pen}} = \vec{0} & \text{if } y + u_y dt > 0 \\ \vec{f_{pen}} = A(y + u_y dt)^2 \cdot \vec{y} & \text{otherwise} \end{cases} \tag{10}$$

A is a penalization constant that needs to be chosen wisely in order to reach convergence. The problem becomes nonlinear with penalization. An iterative Newton-Raphson method is used to solve for $\vec{u}$, p, and $\dot{h}$.

Numerical model validation. The FEM model is validated on two test cases with existing analytical solutions. The first one is a case of simple compression for a Newtonian and a shear-thinning fluid. The second test case is a Newtonian squeeze flow of a rectangular asperity. The numerical degree of intimate contact is calculated from the evaluation of the length in contact with the surface at $y = 0$. For these two test cases, it is considered that $L_\infty = 2L_0$ thus $D_{ic}(t = 0) = \frac{1}{2}$.

For the simple compression case, the asperity geometry is a square ($h_0 = L_0$). Fig. 5 shows agreement between the analytical and numerical solutions of D_{ic} and $\dot{h}$ for simple compression whether the fluid is considered Newtonian or non-Newtonian. For the second test case, in order to compare the numerical solution with Lee and Springer's analytical solution, the dimensions of the rectangle must comply with the lubrication assumption. This implies that the aspect ratio $h(t)/L(t)$ is smaller than unity at each timestep. In this example, the initial width of the rectangle L_0 is equal to 5 and the initial height h_0 is equal to 1. Fig. 6 shows the results for D_{ic} and $\dot{h}$.

In addition, it is possible to determine the numerical evolution index α of Eq. 9 by identifying the slope of the curve of $\dot{D}_{ic}$ as a function of D_{ic} in a log-log graph, represented in Fig. 7a. In order to find the numerical $\dot{D}_{ic}$, the curve of D_{ic} is first fitted with a polynomial regression. The order of the polynomial fit is determined with the minimization of the residual sum of squares (RSS). The polynomial fit is then differentiated to get the numerical $\dot{D}_{ic}$.

In Fig. 7a, the first part of the logarithm curve represents only a few computed points. These points represent the initial contact-and-penalization phase and thus differ from the expected slope. The slope of the main part of the fitted curve is close to the analytical one ($\alpha = -4$), validating this test case. The decrease of the slope at the end of the graph stems from fitting artifacts. By considering that the beginning of the squeeze flow takes place when the evolution index gets close to $\alpha = -4$, at $\log(D_{ic}) = -0.25$, which means at $D_{ic} = 0.56$, the curve of D_{ic} is closer to the analytical solution, as presented in Fig. 7b.

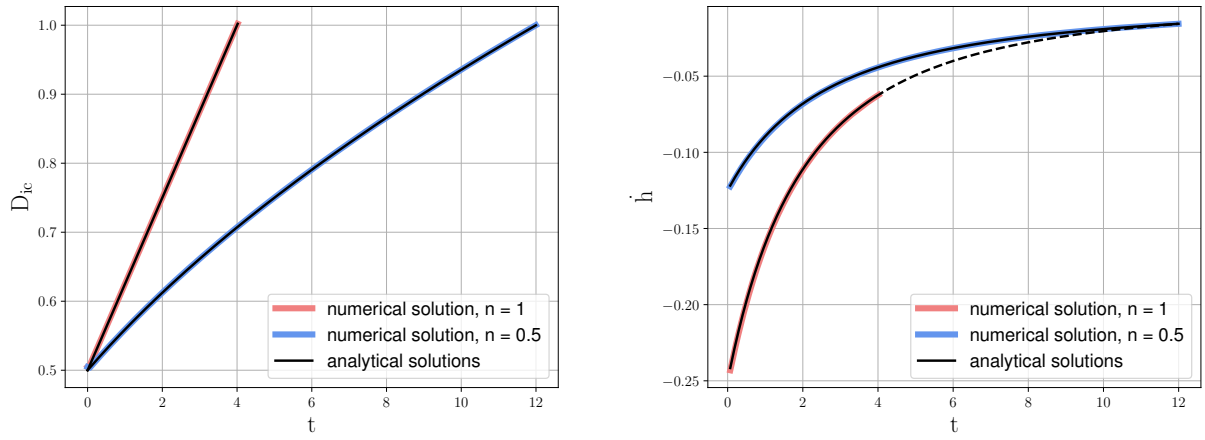

(a) (b)

Fig. 5: (a) Simple compression test case: evolution of D_{ic} as a function of time for different flow behavior index. (b) Simple compression test case: evolution of $\dot{h}$ as a function of time for different flow behavior index.

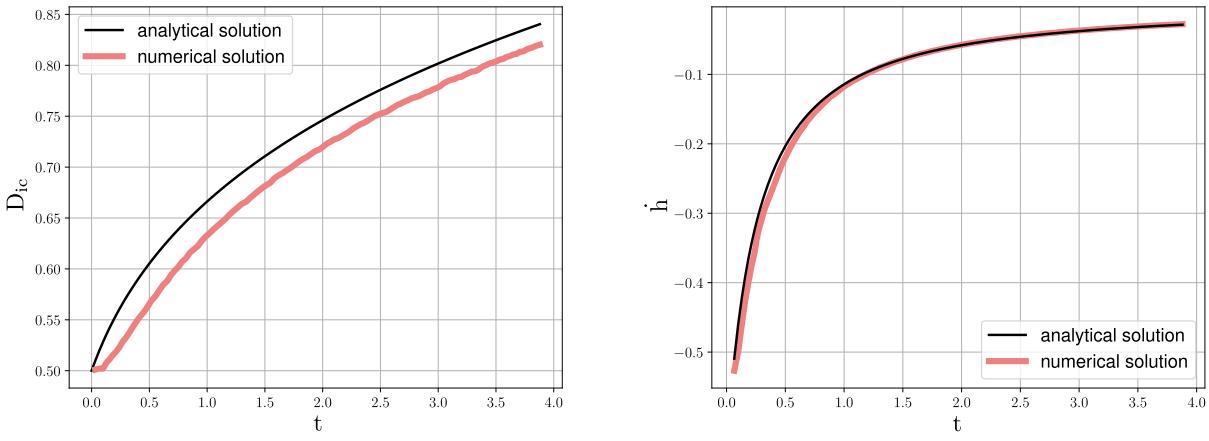

(a) (b)

Fig. 6: (a) Squeeze flow test case: evolution of D_{ic} as a function of time for a Newtonian fluid. (b) Squeeze flow test case: evolution of $\dot{h}$ as a function of time for a Newtonian fluid.

Results and Discussion

Impact of the aspect ratio of a rectangular shape on the prediction of the degree of intimate contact. To describe the material roughness as rectangles, geometrical parameters representing a statistical height and width have to be measured, commonly by profilometry analyses [17, 18, 19]. This section investigates the impact of the aspect ratio (i.e. the ratio between height and width of the statistical rectangle) on the predicted value of D_{ic} compared to analytical solution based on lubrication assumption. It has been observed that for high aspect ratios ($h_0 \approx L_0$), the solved velocity $\dot{h}$ differs from the analytical solution, as presented in Fig. 8a. Consequently, D_{ic} will also vary. They differ at the start of the squeeze flow: when the rectangle get squeezed, the aspect ratio decreases and the numerical solution thus tends toward the analytical solution. The comparison of numerical and analytical $\dot{h}$ is done by calculating the average relative error, $\bar{e}$, for multiple aspect ratios. The average relative

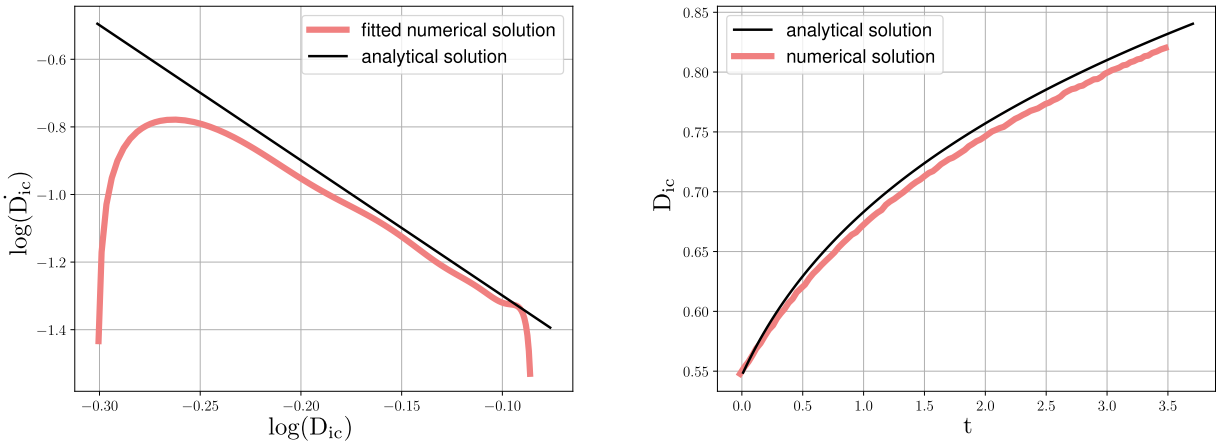

(a) (b)

Fig. 7: (a) Evolution of the logarithm of $\dot{D}_{ic}$ as a function of the logarithm of D_{ic}. (b) Adjusted evolution of D_{ic} as a function of time for a Newtonian fluid.

error is defined as

$$\bar{e} = \frac{1}{t_{sim}} \int_0^{t_{sim}} \frac{|\dot{h}_{num}(t) - \dot{h}_{ana}(t)|}{|\dot{h}_{num}(t)|} dt \tag{11}$$

where t_{sim} is the time reached at the end of the simulation for each case. The results are presented in Fig. 8b.

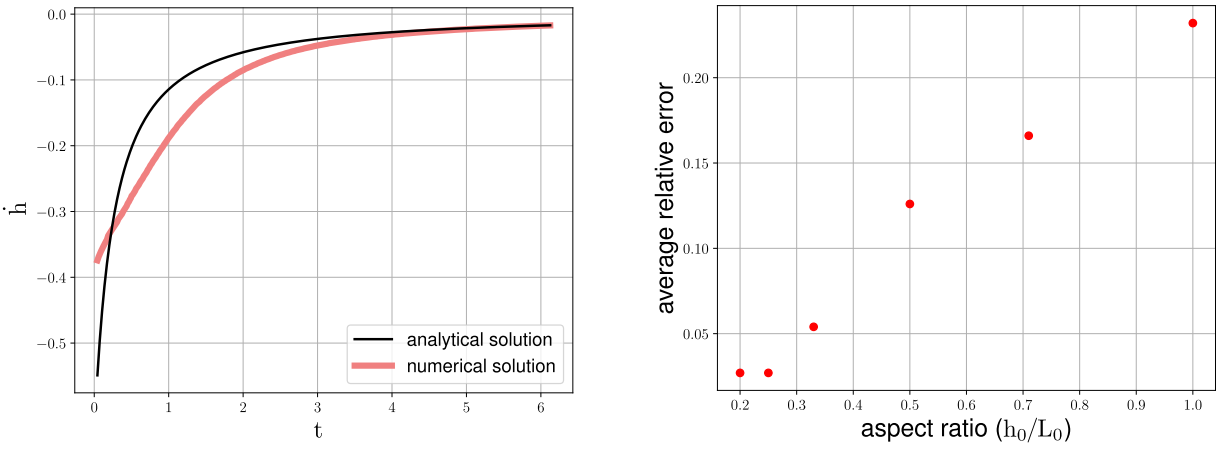

(a) (b)

Fig. 8: (a) Evolution of $\dot{h}$ as a function of time for a rectangular Newtonian squeeze flow with an aspect ratio of 1 : $L_0 = h_0 = 1$. (b) Average relative error with corresponding analytical solutions for aspect ratios between 0.2 ($L_0 = 5h_0$) and 1 ($L_0 = h_0$).

This section shows that the error on $\dot{h}$, and thus on D_{ic}, increases with respect to the aspect ratio, compared to the analytical solution of Lee and Springer's model. When using this analytical model, one must choose a small aspect ratio. Additionally, high incertitude is present when measuring experimentally h_0 and L_0, which may also lead to errors in the prediction of the degree of intimate contact if the aspect ratio is too high, typically above 0.3.

Influence of asperity geometry on the establishment of the degree of intimate contact. Rectangles may not be representative of the real roughness of molten polymers. The finite element model enables to evaluate the establishment of the degree of intimate contact for different asperity geometries, such as trapeze, triangle, half-circle, or even real roughness extracted from profilometry.

In this section, the influence of the asperity geometry is studied by comparing the evolution index α found for a circular shape to the theoretical analytical evolution index given for a rectangular shape, which can be found using Eq. 7 and Eq. 8. Fig. 9a shows the variation of D_{ic} for different flow behaviors. The same procedure as described above in the model validation part is used to fit and find the numerical $\dot{D}_{ic}$. The log-log graph is presented in Fig. 9b. The evolution index is equal to the slope in the log-log graph.

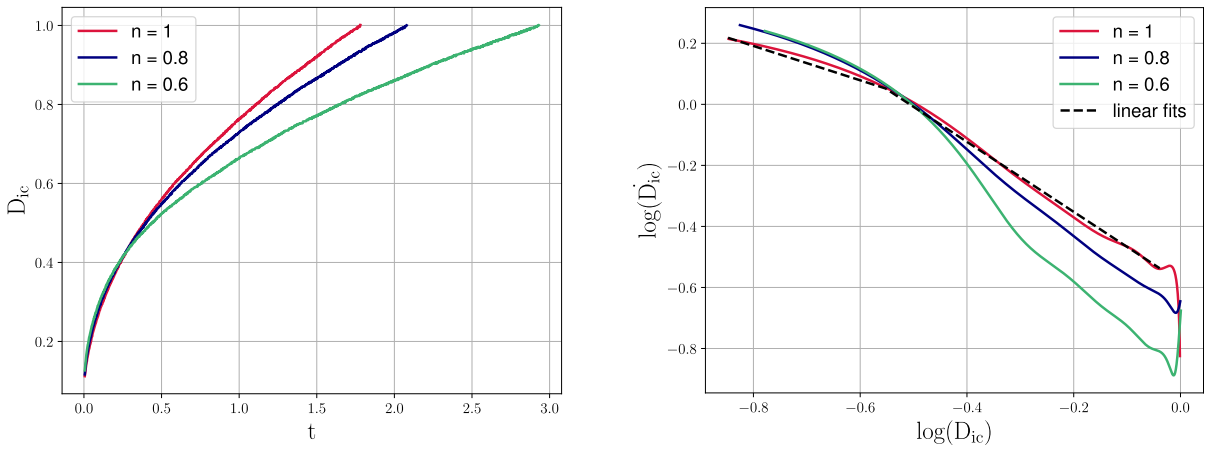

(a) (b)

Fig. 9: (a) Evolution of D_{ic} as a function of time for different flow behavior indices. The geometry considered is a half-circle. (b) Evolution of the logarithm of $\dot{D}_{ic}$ as a function of the logarithm of D_{ic}. The linear fits are plotted as a reference for $n = 1$.

For this particular case, three stages are identified for each curve, based on Fig. 9b. Only the slopes with negative values will be considered; the third one, at the end of the plot, is due to fitting artifacts. Two evolution indices are then identified for each curve. Table 1 summarizes the obtained evolution indices compared to analytical theory for a rectangle. During the first stage, half-circle flow tends to behave closer to a rectangular simple compression (α_1 index). During the second stage, the flow behavior changes to reach an evolution index (α_2) closer to rectangular squeeze flow.

For each type of asperity geometry, the variation of the evolution index enables to estimate a critical transition time, t_{crit}, at which flow behavior changes. This change is accompanied by a switch of morphology for the geometry: from its nearly initial form to a quasi-rectangular constrained shape, as shown for a Newtonian squeeze flow of a triangle in Fig. 10.

In this section, results show that asperities with non-rectangular geometry behave differently than the analytical models. For the two non-rectangular geometries (half-circle and triangle) studied, it is possible to see that the evolution index decreases during the flow. This can be interpreted as a transition from a behavior similar to rectangular simple compression to an intermediate rectangular squeeze flow behavior.

Conclusion

This paper has focused on the study of the intimate contact phenomenon in fast manufacturing processes of thermoplastic composites. Typically, strong hypotheses are made to obtain rectangular squeeze flow analytical models for intimate contact. A more realistic finite element model has been developed based on Stokes flow for Newtonian and shear-thinning fluids in 2D. This numerical model was

Table 1: Evolution indices for rectangular analytical simple compression and squeeze flow. These indices are compared to those from numerical results of the flow of a semi-circular geometry. The field displayed for the semi-circular asperity is the horizontal velocity of the fluid.

flow index	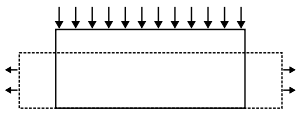 rectangular simple compression	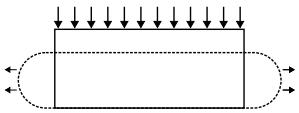 rectangular squeeze flow	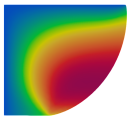 semi-circular flow
n = 1	$\alpha = 0$	$\alpha = -4$	$\alpha_1 = -0.56$ $\alpha_2 = -1.14$
n = 0.8	$\alpha = -0.25$	$\alpha = -4.75$	$\alpha_1 = -0.63$ $\alpha_2 = -1.32$
n = 0.6	$\alpha = -0.67$	$\alpha = -6$	$\alpha_1 = -0.82$ $\alpha_2 = -1.77$

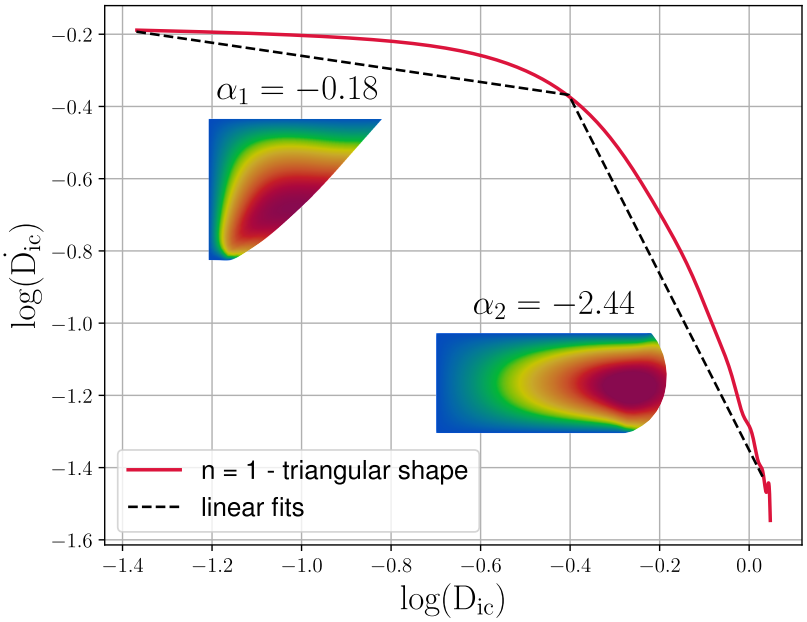

Fig. 10: Transition of the evolution index for a Newtonian triangular flow. A visual representation of the triangle is presented for each evolution index. Similar to the semi-circular flow, the two phases describe two different behaviors during the flow. The field displayed for the triangular asperity is the horizontal velocity of the fluid.

validated on test cases. The first section presents the impact of the asperity aspect ratio on the final degree of intimate contact. As the aspect ratio increases, the error with the uniform rectangle model also grows. Geometrical dependency was shown by comparison of theoretical and numerical evolution indices. This approach appears useful to analyze the flow behavior and could potentially help build a metamodel. Future work will focus on the addition of other physical and chemical phenomena, such as air trapping and wetting. The influence of shear-thinning fluid behavior and the impact of real geometries must be studied further. The intimate contact model must also be experimentally validated.

Acknowledgments

The authors would like to acknowledge the funding of the PERFORM program by IRT Jules Verne (French Institute for Advanced Research and Technology in Advanced Manufacturing Technologies for Composite, Metallic, and Hybrid Structures), which made this work possible. The authors also wish to thank the industrial partners of PERFORM for this project: Airbus, Chantiers de l'Atlantique, Daher, Naval Group, and Safran.

References

[1] U. K. Vaidya and K. K. Chawla. Processing of fibre reinforced thermoplastic composites. *International Materials Reviews*, 53(4):185–218, July 2008.

[2] C. Ageorges, L. Ye, and M. Hou. Advances in fusion bonding techniques for joining thermoplastic matrix composites: a review. *Composites Part A: Applied Science and Manufacturing*, 32(6):839–857, June 2001.

[3] P. G. De Gennes. Reptation of a Polymer Chain in the Presence of Fixed Obstacles. *The Journal of Chemical Physics*, 55(2), July 1971.

[4] R. P. Wool and K. M. O'Connor. A theory crack healing in polymers. *Journal of Applied Physics*, 52(10):5953–5963, October 1981.

[5] Julien Avenet, Arthur Levy, Jean-Luc Bailleul, Steven Le Corre, and Jérôme Delmas. Adhesion of high performance thermoplastic composites: Development of a bench and procedure for kinetics identification. *Composites Part A: Applied Science and Manufacturing*, 138:106054, November 2020. Publisher: Elsevier.

[6] Raphaël Arquier, Ilias Iliopoulos, Gilles Régnier, and Guillaume Miquelard-Garnier. Consolidation of continuous-carbon-fiber-reinforced PAEK composites: a review. *Materials Today Communications*, 2022.

[7] Philip H. Dara and Alfred C. Loos. Thermoplastic Matrix Composite Processing Model. *Virginia Polytechnic Institute and State University, Blacksburg, Virginia*, September 1985.

[8] Woo Il Lee and George S. Springer. A Model of the Manufacturing Process of Thermoplastic Matrix Composites. *Journal of Composite Materials*, 21(11):1017–1055, November 1987.

[9] F Yang and R Pitchumani. A fractal Cantor set based description of interlaminar contact evolution during thermoplastic composites processing. *Journal of Materials Science*, 36, 2001.

[10] Pavel Simacek, Navid Niknafs Kermani, and Suresh G. Advani. A comprehensive framework for modeling volatile transport and bubble dynamics in liquid composite molding processes. *Composites Science and Technology*, 269:111254, August 2025.

[11] Joseph Kirchhoff, Omar Ghattas, and Mehran Tehrani. Resin percolation and intimate contact in fast processing of thermoplastic composites. *Composites Part A: Applied Science and Manufacturing*, 182:108145, July 2024.

[12] A. Arefmanesh, S. G. Advani, and E. E. Michaelides. A numerical study of bubble growth during low pressure structural foam molding process. *Polymer Engineering & Science*, 30(20):1330–1337, October 1990.

[13] John Tierney and John W. Gillespie. Modeling of Heat Transfer and Void Dynamics for the Thermoplastic Composite Tow-Placement Process. *Journal of Composite Materials*, 37(19):1745–1768, October 2003.

[14] Christine A. Butler, Roy L. McCullough, Ranga Pitchumani, and John W. Gillespie. An Analysis of Mechanisms Governing Fusion Bonding of Thermoplastic Composites. *Journal of Thermoplastic Composite Materials*, July 1998.

[15] Susan C. Mantell and George S. Springer. Manufacturing Process Models for Thermoplastic Composites. *Journal of Composite Materials*, 26(16):2348–2377, January 1992.

[16] J. A. Greenwood and J. B. P. Williamson. Contact of nominally flat surfaces. *Proceedings of the Royal Society of London. A. Mathematical and Physical Sciences*, 295(1442):300–319, December 1966.

[17] W.J.B. Grouve, L.L. Warnet, B. Rietman, H.A. Visser, and R. Akkerman. Optimization of the tape placement process parameters for carbon–PPS composites. *Composites Part A: Applied Science and Manufacturing*, 50:44–53, July 2013.

[18] PM. Schaefer, T. Guglhoer, MGR. Sause, and K. Drechsler. Development of intimate contact during processing of carbon fiber reinforced Polyamide-6 tapes.

[19] Arash Khodaei and Farjad Shadmehri. Intimate contact development for automated fiber placement of thermoplastic composites. *Composites Part C: Open Access*, 8:100290, July 2022.